Effect of Zr on the high cycle fatigue and mechanical properties of Al-Si-Cu-Mg at elevated temperatures

Guangyu Liu [1], Paul Blake[2], Shouxun Ji[1,*]

[1] Brunel Centre for Advanced Solidification Technology (BCAST), Brunel University London, Uxbridge, Middlesex, UB8 3PH, United Kingdom

[2] Engineering Centre, Jaguar Land Rover, Abbey Road, Coventry CV34 4LF, United Kingdom

*Corresponding author. Tel.: +44-1895-266663; Fax: +44-1895-269758; E-mail address: shouxun.ji@brunel.ac.uk

Abstract

The Zr-modified Al-Si-Cu-Mg alloy with 0.14wt%Zr addition was studied against the counterparts of commercially used EN-AC-42000 (Al7Si0.5Cu) baseline alloy for the effect of Zr on the high cycle fatigue (HCF) and mechanical properties at elevated temperatures of 150, 200, 250 ^{o}C. It was found that the fatigue life was significantly improved by 8-10 times at the high stress amplitude of 140 MPa in the Zr-modified alloy at all different temperatures. The fatigue strength coefficient, σ_f', of the baseline alloy was 574.9, 589.8, and 514.8 MPa at 150, 200, and 250 ^{o}C, respectively, which was greatly increased to 1412.3, 620.1, and 821.6 MPa for the Zr-modified alloy. The tensile strength was considerably improved by 34%-50%, dependant on the testing temperatures. The improved fatigue and tensile properties in the Zr-modified alloy could be mainly ascribed to: (1) the refined microstructure, with α-Al grain size decreasing from 335 to 253 μm and the secondary dendrite arm spacing (SDAS) dropping from 39 to 28 μm; (2) the reduced porosity; and (3) the additional precipitates strengthening effect by the nano-sized Al-Si-Zr-Ti dispersoids.

Keywords: aluminium alloys; microstructure; mechanical properties; fatigue properties; defects.

1. Introduction

Al-Si-Cu-Mg cast aluminium alloys have gained a growing interest for the application in automotive engine powertrains, such as cylinder heads and engine blocks, due to their high strength-to-weight ratio, excellent thermal stability, and good castability [1, 2]. Modern automotive engines have been confronted with an increasingly great challenge of improving efficiency and overall mechanical performance. In theory, increasing the maximum operating temperature and pressure of engines can effectively improve the efficiency of the engine. However, the increased temperature and pressure will undoubtedly pose a considerable demand for the improved mechanical performance of aluminium alloys at elevated temperatures. During operation, the cylinder head works continuously at a high temperature and thermal cyclic stress condition at numerous start-stop cycles [3]. Each cyclic loading will cause periodic stress in the casting parts [4]. Therefore, fatigue behaviour at elevated temperatures becomes a major consideration in the design of engine products.

The fatigue behaviour of Al-Si-Cu-Mg alloys is affected by various factors which include casting defects such as the porosities and oxide inclusions [5], secondary dendrite arm spacing (SDAS) [1, 6], Si particles [7], and the Fe-rich intermetallic phases [8]. Overall, the microstructure exhibiting lower porosity volume fraction, finer SDAS, less brittle intermetallic phases, as well as higher Si modification causes better fatigue resistance [6]. Notably, the precipitate strengthening that is strongly responsible for enhancing the strength can play key roles in improving the fatigue resistance of aluminium alloys. For the application of cylinder heads, the main challenge lies that the strength of heat treatable cast Al-Si-Cu(Mg) alloys decreases at temperatures above about 200 ^{o}C [9]. Dispersoids like β-Mg_2Si that maintain the high strength of the alloy usually coarsen or dissolve at temperatures above 200 ^{o}C, resulting in decreased fatigue resistance at high temperatures and consequently causing a considerable decline of engine performance [10].

A trace of the transition alloying element(s) such as Mn, Mo, Ni, Cr, V, Zr, and Ti are often added to Al-Si-Cu-Mg alloys to maintain/improve the fatigue and mechanical properties at high temperatures, because these elements: (1) can form thermally stable strengthening phases such as Al_3Zr; (2) have low solid solubility and exhibit low diffusivity in the Al matrix; (3) can retain the ability for the alloy to be conventionally solidified. Shaha et al. [11, 12, 13] have extensively studied the effect of Mn, Mo, Ti, V, and Zr on the mechanical properties of Al-Si-Cu-Mg. It was found that the addition of Mn and/or Mo significantly improved the tensile and low cycle fatigue (LCF) properties of Al-7Si-1Cu-0.5Mg under T6 peak aging condition, leading to the 7% higher of UTS and 16% higher of elongation due to the formation of Mn- and Mo-rich dispersoid precipitates [11, 12]. Elhadari et al. [9] proposed that Ti, Zr, and V enhanced the tensile and low cycle fatigue properties of Al-7Si-1Cu-0.5Mg, with 60-87% increment in the yield strength. Also, a small amount (<0.5wt%) of Ti, V, and Zr was proved to improve the high-temperature low cycle fatigue behaviour of the T6 heat treated Al-7Si-1Cu-0.5Mg alloy [10, 13]. Feng et al. [14] reported that Ni additions (1-4wt%) were beneficial to the tensile and LCF properties of Al-12Si-0.9Cu-0.8Mg alloy at 350 ^{o}C, due to the formation of Al_3Ni phase. Hernandez-Sandoval and Mohamed proposed that additions of Ti, Zr, and Ni in the Al-Si-Cu-Mg alloy could improve their high temperature strength [15, 16]. In addition, our previous work [17] have confirmed that the 0.2wt% Zr addition can improve the mechanical properties of Al-7Si-0.5Cu-Mg both at room and elevated temperature (200 ^{o}C).

Despite the relative studies regarding the influence of Zr on the mechanical properties of Al-Si-Cu-Mg alloys [9, 10, 13], the information for the effect of Zr on high cycle fatigue (HCF) properties remains limited. Besides, it is still unclear how Zr modify the Al-Si-Cu-Mg cast alloys with relatively high Si and Cu. Therefore, in the present study, the Zr-modified Al-Si-Cu-Mg alloy with 0.14wt%Zr addition was studied against the counterparts of commercially used EN-AC-42000 (Al7Si0.5Cu) baseline alloy for the effect of Zr on the high cycle fatigue

(HCF) and mechanical properties of Al-Si-Cu-Mg alloy at elevated temperatures of 150, 200, 250 ^{o}C. The metallurgical microstructure features including α-Al grains, SDAS, eutectic Si particles, and porosities were thoroughly examined. The discussion focused on the effect of Zr addition on the microstructure refinement and the microstructure-mechanical property relations.

2. Experimental

Commercially pure Mg and Cu ingots, combined with Al-50Si, Al-10Sr, Al-10Ti, and Al-10Zr master alloys were added to a standard A356 alloy (Al7Si0.3Mg), to prepare the baseline and Zr-modified Al-Si-Cu-Mg alloys with the chemical compositions (in weight) reported in Table 1. The A356 alloy and master alloys were melted in the electrical resistance furnace (Carbolite) at 750 ^{o}C. When the melt was homogenised after hold for approximately 2 hours, Al-10Sr master alloy was added to the melt to modify the morphology of the eutectic Si particles during solidification. Then, the melt was subjected to degassing, during which argon was blown into the melt by using a rotatory degasser at a rotating speed of 350 rpm for 6 min. After degassing, the melt was covered by a commercial granular flux on the surface, and hold for 15 min for temperature rise. Thereafter, the melt was poured at 730 ^{o}C into a permanent steel mould, pre-heated to 460 ^{o}C, to produce the cylinder-shaped casting bars with 20 mm in diameter and 165 mm in length. The casting bars were heat treated subjected to T6 heat treatment involving the solutionizing at 535 ^{o}C for 8 hours, followed by immediate water quenching to room temperature, and then artificial aging at 170 ^{o}C for 8 hours, followed by air cooling to room temperature.

The mechanical test was performed on the specimens with a circular cross section, extracted from the central part of the cylinder-shaped casting bars. The tensile test was conducted at room and elevated temperatures using Instron 5500 universal Electronmechanical Testing System

equipped with Bluehill software and a 50 KN load cell. Room and elevated temperature tensile tests were performed according to ASTM E8/E8M [18] and ASTM E21 [19], respectively. A gauge length of 50 mm and a gauge diameter of 10 mm were applied. Each data reported with standard deviation was based on the mechanical properties attained from 6 to 8 samples. The high cycle fatigue test was carried out on a 10 kN MTS-810 servohydraulic test machine equipped with a heating chamber at 150, 200, and 250 ^{o}C according to ASTM E466-15 [20]. The geometry and dimension of the sample for HCF tests were shown in Figure 1. Prior to tests, the specimen was preheated in the heating chamber and held for 30 min to ensure sample temperature uniformity. A sinusoidal waveform was used under fully-reversed stress-controlled conditions. The test was performed with a constant stress amplitude in the range of 60-160 MPa, with stress ratio R= -1 and test frequency of 40 Hz. The test was continuously running until the full fracture of specimens or reached 1.0×10^{7} cycles without fracture.

The metallographic microstructural examination was conducted on the cross section of testing bars at the gauge position. The surface to be examined was ground using SiC abrasive papers and then polished using silica suspension (OPS, 0.05μm water based SiO_2 suspension). The electrochemical etching was applied on the polished surface to reveal the dendrite and grain structure, with the etching solution of Baker's etchant (200 ml H_2O and 10 ml 35vol% Fluoroboric acid). Grain structure characterisation was performed using Zeiss Scope A1 optical microscope in polarised mode. Quantitative analysis of the microstructure was performed using AxioVision Rel. 4.8 software. Detailed information on intermetallic phases and fractured surfaces was obtained using the Zeiss Supra 35 field-emission scanning electron microscope (FESEM), equipped with energy dispersive X-ray spectroscopy (EDS). Nano-scaled precipitates were examined using high resolution transmission electron microscopy, JEOL 2100F (JEOL Ltd.). The TEM samples were cut from the T6 heat treated baseline and Zr-modified specimens and were ground to less than 100 μm thicknesses. 3 mm diameter samples

were punched, and the further reduction of thickness was obtained by Gatan precision ion polishing system (PIPS) adjusted at 5.0 kV and at an incident angle of 4°.

3. Results

3.1 Microstructure characterization

Figure 2 compares the grain size variation between the baseline and Zr-modified Al-Si-Cu-Mg alloys after T6 heat treatments. It was observed that the Zr-modified alloy exhibited a smaller grain size than that of the baseline alloy. The average α-Al grain size of the baseline alloy was measured 335 ±18 μm, which was decreased by 24%, to 253±41 μm for the Zr-modified alloy. Figure 3 shows the morphology, size, and distribution of the primary α-Al phase, eutectic, and Si particles in the microstructure of baseline and Zr-modified alloys. Clearly, both alloys were characterized by α-Al dendrites and eutectic Si particles. It is seen from Figure 3a and 3c that the baseline alloy exhibited relatively long α-Al dendrites with the statistically measured secondary dendrite arm spacing (SDAS) of 39 μm, while the Zr-modified alloy highlighted more dendrites with globular rosette morphology, displaying a decreased SDAS value of 28 μm. Also, a more fraction of Al-Si eutectic was observed in the microstructure of the Zr-modified alloy (33.1%) compared with that of baseline alloy (27.9%). This was because more Si contents was added in the Zr-modified alloy. The higher-magnification micrographs characterized the size and morphology of eutectic Si particles, showing no significant difference in the morphology and dimension of Si particles between the two studied alloys (Figure 3b and 3d).

To quantitatively analyse the size and morphology of eutectic Si, more than 10000 individual Si particles for each alloy were statistically measured. The particle size distributions of Si are shown in Figure 4, in which Figure 4a and 4b shows the variation of number fraction and area fraction with the Si particle sizes, respectively. It is seen that the Si particles in the two alloys

displayed an undistinguishable variation trend of frequency with the particle sizes (Figure 4a). The Si particles with the Ferret diameter in the range of 1-12 μm took up most of the total number, and those with the Ferret diameters of 4 μm accounted for the pick proportion, about 21%. The mean Ferret diameter of the baseline alloy and Zr-modified alloy was measured as 3.3 μm and 3.1 μm, respectively, indicating a decrease, but very limited extent, in Si particle size after Zr modification. On the contrary, the variation of area fraction of Si particles between the two alloys saw a relative difference, as shown in Figure 4b. The Si particles with the sizes of approximately 5 μm accounted for the highest area proportion of the total Si area, exhibiting the pick value of 17.5% and 22.3% for baseline and Zr-modified alloys, respectively. The coarser (> 12 μm) Si particles represented less area fraction in Zr-modified alloy in comparison with the baseline alloy. This indicated that fine Si particles (<12 μm) contributed more to the entire area of Si particles in the Zr-modified alloy compared with those in the baseline alloy. It might be thus induced that Zr-modified alloy had more fine Si particles.

Figure 5 shows the aspect ratio distribution of Si particles in the baseline and Zr-modified alloys. The Si particles presented a very similar variation trend of frequency with Si particle aspect ratios in both alloys, despite the slight higher pick value for the Zr-modified alloy. The mean aspect ratios were measured 1.65 and 1.61 for the baseline and Zr-modified alloy, respectively, indicating the indistinguishable aspect ratio of Si particles in the two studied alloys.

Figure 6 presents the optical micrographs showing the morphology and size of porosities in the microstructure of the baseline and Zr-modified alloys. Both shrinkage pores and gas pores were observed in both alloys. The quantitative analysis on the size, morphology, and area fraction of the porosities was conducted by statistically measuring numerous porosities in different cross sections, as summarized in Table 2. For the baseline and Zr-modified alloys, the area fractions of porosities were 0.33% and 0.31%, the mean aspect ratios of porosities were 2.4

and 2.0, and the porosity sizes (Ferret diameters) were 110.2 and 106.1 μm. This indicated slight decreased porosity in the Zr-modified alloy.

Figure 7 presents the back-scattered SEM micrographs showing the Fe-rich intermetallic phases in the baseline (Figure 7a and 7b) and Zr-modified (Figure 7c, d, and e) alloys. The corresponding chemical compositions of the individual Fe-rich intermetallic phases highlighted by S1, S2, S3, S4, and S5 were analysed by EDS, as shown in Figure 8. The β-Al_5FeSi phase which exhibited the needle-like morphology was readily observed in both alloys (Figure 7a and 7c), due to their high thermal stability. The π-$Al_8FeMg_3Si_6$ intermetallics (S1 and S4) were perceived to display the block and script morphology, taking up lower proportion compared with the β-Al_5FeSi phase, due to the partial dissolution of the phase under T6 heat treatment [21], as indicated in Figure 7b and 7d. Besides, the α-Al_8Fe_2Si intermetallics were also detected with small amounts in comparison with that of the β-Al_5FeSi and π-$Al_8FeMg_3Si_6$ phases. Same Fe-rich intermetallic phases were observed in the Al-Si-Cu-Mg alloys by others [10, 15]. Note that the Mg- and Cu- rich intermetallic phases, such as Mg_2Si, θ-Al_2Cu and Q-$Al_5Cu_2Mg_8Si_6$, were scarcely detected in both alloys due to their complete dissolution into the Al matrix during solution treatment [22, 23].

In addition, the Zr-containing phase presented in the microstructure of Zr-modified alloy, exhibiting the plate-like morphology with the length of 10-50 μm and the width of several microns, as shown in Figure 7e. The EDS result confirmed that the Zr-containing phase comprised the elements of Al, Si, Zr, and Ti. Based on the ratio of each elements and previous literatures, this phase is very likely $(AlSi)_3(TiZr)$ [16, 10]. The Al-Si-Zr-Ti phase was formed during solidification and could not be dissolved under heat treatment because of its high stability at elevated temperatures [21].

3.2 Tensile properties

Figure 9 shows the tensile properties of the baseline and Zr-modified alloys at room and elevated temperatures (150, 200, and 250 ^{o}C). The detailed data of the yield strength (YS), ultimate tensile strength (UTS), and elongation are summarized in Table 3. Overall, the YS and UTS were decreased constantly and the elongations were increased monotonously as the temperature rose from room temperature (RT) to 250 ^{o}C. This was ascribed to the materials softening on the account of dissolution and coarsening of the strengthening phases. At elevated temperatures, dislocations can bypass the obstacles by climbing, which facilitate and accelerate dislocation gliding and concomitant deformation. Also, a higher number of slip systems can be activated with the increase of temperature [17].

Notably, the strengths of the Zr-modified alloy were much greater than that of the baseline alloy at all range of temperatures. Specifically, at ambient temperature, the YS and UTS of the baseline alloy was 218 and 272 MPa, which was remarkably increased by respective 34% and 37% to 293 and 374 MPa for the Zr-modified alloy. At 150 ^{o}C, the baseline alloy possessed YS and UTS of 181 and 196 MPa, while the Zr-modified alloy had YS and UTS of 264 (46% increment) and 294 MPa (50% increment). At 200 ^{o}C, YS and UTS for baseline alloy was 160 and 173 MPa, remarkedly increased to 232 (by 45%) and 256 MPa (by 48%). The increased strength was mostly attributed to the modified microstructure by Zr additions, which will be discussed afterwards.

3.3 High cycle fatigue

Figure 10 shows the stress-life (*S-N*) curves for the baseline and Zr-modified alloys at 150, 200, and 250 ^{o}C. The relation between stress amplitude (σ_a) and the number of cycles to failure ($2N_f$) was fitted using Basquin's equation [24]: $\sigma_a = \sigma_f' \left(2N_f\right)^b$, where σ_f' refers to the fatigue strength coefficient and b represents the fatigue strength exponent. Overall, when the same

stress amplitude was applied, the Zr-modified alloy could often bear longer fatigue cycles, indicating the better fatigue resistance. Especially when loaded at the higher stress amplitude of 140-160 MPa, the Zr-modified alloy showed 8-10 times longer fatigue lives than the baseline alloy, dependant on stress amplitudes and temperatures. The values for the σ_f' and b of the baseline and Zr-modified alloys were extracted from the *S-N* curves, as indicated in Table 4. It shows that at 150 ^{o}C, 200 ^{o}C, and 250 ^{o}C the respective σ_f' values of the baseline alloy were 578, 589, 515 MPa, which were significantly increased to 1412, 620, and 822 MPa for the Zr-modified alloy. This indicated that the Zr-modified alloy possessed superior fatigue resistance compared with the baseline alloys, at elevated temperatures.

3.4 Fractography

Figure 11 shows the SEM fractography of the baseline alloys subject to HCF testing under the stress amplitudes of 150, 100, and 70 MPa, at 200 ^{o}C. Three distinct zones were clearly perceived, including the fatigue crack initiation (FCI) zone, fatigue crack growth (FCG) zone, and final fracture zone. The FCG zone area was increased constantly with the stress amplitudes decreasing from 150 to 70 MPa, as indicated by dashed white lines shown in Figure 11a, 11c, and 11e. This is indicative that a lower stress amplitude lengthened the crack propagation process and consequently delayed the final rupture process, which was in agreements with the *S-N* result showing that lower stress amplitudes caused longer fatigue lives, as shown in Figure 10b. The regions marked by the yellow rectangles highlighted the FCI zone, with the corresponding magnified image shown in Figure 11b, 11c, and 11d, revealing that the crack initiation occurred exclusively from the pores and inclusions at the vicinity of the surface. These sites could act as stress concentrators facilitating the formation of fatigue cracks [25, 26].

The similar features for the fractographies appeared in the case of Zr-modified alloys after HCF testing at the same stress amplitudes of 150, 100, and 70 MPa at 200 ^{o}C, as shown in Figure 12. The FCG size increased consistently with decreasing the stress amplitude, indicated by the dashed white lines in Figure 12a, 12c, and 12e. The enlarged FCI regions showed that the fatigue crack initiation originated from the porosities and inclusions at the vicinity of the surface (Figure 12b, 12d, and 12f). On comparison of the FCG areas between the two alloys, it was shown that the FCG size was larger in the Zr-modified alloys at each stress amplitude of 150, 100, and 70 MPa (Figure 11 and Figure 12). This might indicate that the Zr-modified alloy exhibited slower fatigue crack growth rates.

Figure 13 presents the higher magnified SEM fractography, showing detailed features of the FCG zones in the baseline and Zr-modified alloy after the fatigue test under the stress amplitude of 100 MPa, at 200 ^{o}C. A great area of fatigue striations and tear ridges were readily observed in the fracture surfaces of both studied alloys, indicative of ductile fracture modes at 200 ^{o}C. It has been well documented that the α-Al belongs to the faced-centred cubic (FCC) lattice, which has a high stacking fault energy with some propagated slipping systems, {111} <110>. Thus, the fatigue striations normally generated in front of the fatigue crack tip in the FCC materials as the result of dislocations in the plastic zone [27]. The fatigue striation propagation oriented along fatigue crack growth direction, as indicated by the yellow arrows in Figure 13. However, in some local regions, the localized FCG directions might be different to the overall crack propagation direction, as shown in Figure 13d, in which a local FCG direction is not in line with the FCG direction shown in Figure 13c. Another typical feature observed was the prominent micro-cliffs along the crack propagation plane (Figure 13b and 13d). These micro-cliffs have a step-like pattern formed inside of the grain parallel to the FCG path, which seems to demonstrate lateral slippage at the crack tips in both alloys [28].

4. Discussion

4.1 Microstructural refinement

A considerable grain refinement was confirmed by the quantitative analysis on the metallurgical microstructure of the baseline and Zr-modified alloys, with the α-Al grain size reduced by 24% (from 335 to 253 μm) and the SDAS decreasing by 28% (from 39 to 28 μm), as indicated in Table 2. Considering that the casting parameters such as the cooling rates for the two studied alloys were the same, the microstructure variation from solidification process was thus negligible. As a result, the effective grain refinement could be ascribed mainly to the chemical composition difference between the two studied alloys, including Cu, Mg, Si, Ti, and Zr elements.

It is known that the effective grain refinement for aluminium alloys is closely related to the solute and nucleant particles [29, 30]. The contribution of solute is associated with the role of solute segregation in front of the liquid-solid interface in restricting growth of grains and developing constitutional undercooling that provides a driving force to activate further nucleation on the substrates present [31]. In the present case, since the Mg and Ti contents in the two studied alloys were almost identical, the increased Cu, Si concentrations and the additional Zr could be the reason for the remarkable decrease in the grain size and SDAS value, due to a stronger solute segregation effect and more nucleant particles in the Zr-modified alloy.

The solute segregation effect is ascribed to the growth rate restriction of the dendrites during solidification, which can be explained using the growth restriction factor, Q [29, 32]. Briefly, Q is regarded as a qualitative index to estimate how fast the liquid ahead of the solidification front becomes constitutionally undercooled in the earliest stages of crystals growth, and can therefore be used as a criterion for the microstructural refinement of Al dendrites. For binary alloys, such as Al-Si, Al-Cu, and Al-Zr, it is defined by $Q = m(k-1)c_0$, in which m is the

slope of the liquidus, k is the partition coefficient, and c_0 is the initial concentration of the solute [33]. In multicomponent alloys, the use of growth restriction factor could be critical, especially in the case of strong solute-solute interactions. However, it has been reported that, for dilute alloys (the studied alloys are the case in terms of Cu and Zr contents), the actual growth restriction factor could be estimated by summing the contribution of each solute independently, without interaction terms [34]. It is known that Q is inversely proportional to the growth rate of α-Al crystals [34]. A higher amount of solute, e.g. Cu, Si, Zr, can result in a larger value of Q and a lower dendrite growth rate, which consequently lead to a finer α-Al dendrite. This is because the solutes accumulation ahead of the solidifying dendrites is responsible for constitutional undercooling at the dendrite tip, retarding the dendritic growth.

However, Wang et al. [35, 36] investigated the influence of eutectic-forming elements (Si, Cu, and Mg) and peritectic-forming elements (Zr, Nb, and Ti) on the grain refinement for aluminium by using the analytical model of grain refinement (the Q-model [29, 32]), suggesting that the addition of Cu (0-4wt%) and Si (0-1.5wt%) to aluminium caused very limited extent of grain refinement; while the addition of Zr and Nb, especially when the concentrations are over the maximum solubility, could cause significant grain refinement. Based on this and considering that the Cu concentrations in the studied alloys were low and that the content differences in Cu and Si between the two studied alloys were relatively small, i.e. 0.3wt% in Cu contents and 1.8wt% in Si contents, it is thus reasonably deduced that the increased Cu and Si contents might be influential, but not much, to the grain refinement. Instead, the additionally added Zr could be attributed to the microstructure refinement, particularly the reduction of SDAS.

As aforementioned, Zr, at first, serving as a certain alloying element, had a relatively positive effect on the grain refinement, especially the SDAS reduction, through the growth rate restriction approach. However, the degree of grain refinement by solute related segregating

power was relatively small as the Zr solute in Al liquid was considerably limited (maximum solubility, c_m, of Zr in Al is 0.11wt% [33]). Because of this, the growth rate restriction factor, Q, was limited to the maximum value of 0.7K, producing small degree of grain refinement. Nevertheless, once the Zr addition was over 0.11wt.% (c_m in Al), a significant grain refinement could be achieved by additional Zr which due to the formation of the pro-peritectic particles (Al_3Zr, for instance), which was believed to be beneficial to the heterogeneous nucleation, resulting in significant grain refinement. In the present study, although no Al_3Zr pro-peritectic particles were identified in the Zr-modified alloy, the Zr-containing pro-peritectic Al-Si-Zr-Ti intermetallics were readily observed (Figure 7) and it was highly possible for them to act as heterogeneous nucleation points for the Al dendrites. This was reported by others [37].

The quantitative analysis of eutectic Si particles revealed that Zr had no evident effect on the Si particle size and aspect ratio, since their values maintained almost constant in the two studied alloys, as shown in Table 2. A higher fraction of eutectic regions was observed in the Zr-modified alloy, due to more Si contents added. Further analysis on the characteristic of porosities in both alloys suggested that Zr addition seemed to have a positive effect on reducing the porosity, despite of the very limited extent. The mean aspect ratio and the mean Ferret diameter of the porosities were also reduced in the Zr modified alloy. This was attributable to the grain refinement. A finer microstructure could be beneficial to the reduction of the porosity [38].

4.2 Tensile and high cycle fatigue properties

It has been evidenced that the tensile strengths of the Zr-modified alloys were superior to the baseline alloys at all test temperatures of 150, 200 and 250 ^{o}C. This could be mainly attributed to the following reasons. First, the Zr-modified alloy possessed finer primary α-Al dendrites and SDAS compared with the baseline alloy (Table 2). According to Hall-Petch relation [39,

40], the finer grains brought more grain boundaries which could improve the alloy strength (yield strength and hardness), due to the enhanced boundary strengthening. Second, more eutectic Si particles in the Zr-modified alloy intensify the effect of secondary phase strengthening, because of the Si particles acting as the barriers for the dislocations motion during straining/deformation.

Significantly, the precipitate strengthening was the dominant strengthening mechanism for the studied Al-Si-Cu-Mg alloys subjected to T6 heat treatments. Figure 14 shows the bright-field TEM micrographs and the EDS analysis of the studied Al-Si-Cu-Mg alloys after T6 heat treatments. Figure 14a presents the TEM micrograph taken along $<001>_{\alpha\text{-Al}}$ axis, showing the β′′, θ′, and Q′ precipitate phases in the baseline alloy, as indicated by the arrows [17, 41]. The corresponding selected area diffraction pattern (SADP) of α-Al matrix and precipitates is shown in Figure 14b, the bright points are diffraction points of α-Al matrix, while the grey cross lines between the bright points are diffraction patterns of precipitates, which demonstrated that the precipitates were in the metastable state and the heat-treated alloy was in the peak strength state [41]. It is noted that the β′′, θ′, and Q′ phases with similar morphologies and sizes were also detected in the Zr-modified alloy which was not presented here. In addition to the β′′, θ′, and Q′ precipitates, the Zr-containing precipitate was readily perceived in the Zr-modified alloy, as shown in Figure 14c and 14d. The EDS analysis confirmed the composition of the Zr-containing precipitate consisting of Al, Si, Zr, and Ti elements (Figure 14e).

The β′′, θ′, and Q′ precipitate phases served as the main strengthening phases to retard dislocation gliding and interacted with dislocations through Orowan strengthening mechanism [42]. The high Cu contents could provide more θ′, and Q′ phases in the Zr-modified alloy, enhancing the precipitate strengthening [43]. Note that the Cu-containing precipitates, particularly the Q′ phase are relatively stable at elevated temperature (<300 ^{o}C) [23], as a result,

it could benefit to the strength at elevated temperatures of 150, 200, and 250 ^{o}C [44]. Most importantly, the addition of Zr has introduced additional Al-Si-Zr-Ti strengthening precipitates, which displayed elliptical morphology with the size of 80-200 nm, as identified here (Figure 14) and in our previous work [17]. The Al-Si-Ti-Zr precipitate showed small diffusivity in Al matrix at elevated temperatures and could largely enhance the mechanical properties of Al-Si-Cu-Mg alloys at high temperatures [17].

It is generally accepted that the resistance to monotonic loading, to a large extent, determine the ability of the material to resist cyclic loading, when no obvious casting defects like porosity and oxides presented. The fatigue strength of Zr-modified alloys were much better than that of the baseline alloys at all temperatures of 150, 200, and 250 ^{o}C, as shown in Figure 10 and Table 4. For instance, notably, at 200 ^{o}C, the fatigue life of Zr-modified alloys was measured almost ten times longer than that of the baseline alloys at all stress amplitude levels (Figure 10b). This could be greatly related to the boosted precipitate strengthening effect caused by higher amount of Cu-containing precipitates and additional Al-Si-Zr-Ti precipitates, which improved the resistance to dislocation gliding during cyclic straining through Orowan strengthening effect.

The fatigue life is primarily spent by the fatigue crack initiation and crack propagation processes in HCF tests [45]. When the porosity presents, the porosity has the most detrimental effect on fatigue properties, especially when porosities display in large numbers, dimensions, and complex shapes, because of the high stress/strain concentrations near the porosity [46, 47]. When the number and the size of porosities remain below a critical level, oxide inclusions become the next operational mechanism in the hierarchy [48]. This was well evidenced by the fracture surface features, showing that the crack initiated exclusively from the shrinkage porosity and/or inclusions, as indicated in Figure 11 and Figure 12. The Ferret sizes of the porosities where cracks initiated were smaller in the Zr-modified alloy at all stress levels of 150, 100, and 70 MPa. From Table 2, it is shown that the area fraction, mean Ferret diameter,

and mean aspect ratio of the porosity in the Zr-modified alloy exhibited lower values compared to the baseline alloy. The reduced porosity in Zr-modified alloys was closely associated with the reduced grain size and finer SDAS, which was believed to be beneficial to the reduction of porosity [45]. It is worthy noted that the maximum size of the porosity was more detrimental than the mean size of the porosity [46]. This could be indirectly evidenced by the fact that the Ferret size of the porosity where the crack initiated was approximately 472, 727, 547 μm at the stress amplitudes of 150, 100, and 70 MPa at 200 ^{o}C (Figure 11) for the baseline alloy, on the contrary, these values were reduced to 411, 352, 402 μm, respectively, for the Zr-modified alloys when tested at same stress states (Figure 12).

Upon initiation, the crack propagated under the cyclic stress/strain, across the α-Al dendrites and eutectic regions. Microstructural features including the α-Al matrix, SDAS, porosity, and Si particles play roles in the crack propagation process. As aforementioned, the strengthened α-Al matrix by solute solution and precipitates could boost the resistance to the motion of the crack tip. In addition, the size and morphology of Si particles affected the fatigue crack growth characteristics of cast Al-Si alloys [49]. Fine Si particles (<2.5 μm) resulted in decohesion of the particle/matrix interface, coarse Si particles (5.5-9 μm) generally caused cleavage crack growth, while the intermediate size range of Si particles (2.5-5.5 μm) could give rise to both particle cleavage and decohesion. Also, the Si particles with large aspect ratio could result in higher strain/stress concentration and cause easier breakup or decohesion. The Si particle sizes in the studied alloys were similar, approximately 3 μm, exhibiting undistinguishable variation, and the aspect ratios were also similar, indicating that the effect of morphology and the size of the Si particles may not cause a significant difference of crack propagation.

5. Conclusions

The Zr-modified Al-Si-Cu-Mg alloy with 0.14wt%Zr addition was studied against the counterparts of commercially used EN-AC-42000 (Al7Si0.5Cu) baseline alloy for the effect of Zr on the high cycle fatigue and tensile properties at elevated temperatures of 150, 200, 250 ^{o}C. The microstructural features and mechanical properties of the alloys subject to T6 heat treatments were thoroughly studied. Main conclusions can be drawn as follows:

(1) The addition of Zr significantly refined the microstructure of Al-Si-Cu-Mg baseline alloy, with the α-Al grain size decreasing from 335 to 253 μm and the SDAS decreasing from 39 to 28 μm. The microstructure refinement could be resulted from the solute segregation effect and the heterogeneous nucleation via pro-peritectic Zr-containing phase serving as the effective nucleant particles. The eutectic Si particles in both studied alloys displayed no distinct differences in terms of the size and morphology, with the diameter of approximately 3.3 μm and mean aspect ratio of 1.65. The area fraction, aspect ratio and the size of porosities were slightly reduced by Zr addition, while the measured maximum size of porosity was largely decreased.

(2) The fatigue property was considerably improved by addition of Zr, with the fatigue life increased by almost 8-10 times at the stress amplitude of 140-160 MPa for all temperature conditions. The fatigue strength coefficient of the baseline alloy was 574.9, 589.8, and 514.8 MPa at 150, 200, and 250 ^{o}C, respectively. The respective value was significantly increased to 1412.3, 620.1, and 821.6 MPa in the Zr-modified alloy.

(3) Tensile results showed that the strengths were remarkedly improved after addition of Zr. At room temperature, the yield strength (YS) and ultimate tensile strength (UTS) of the baseline alloy was respective 218 and 272 MPa, which was substantially increased by 34% and 37%, respectively, to 293 and 374 MPa for the Zr-modified alloy. At 150 ^{o}C, the YS and UTS was increased by 46% (from 181 to 264 MPa) and 50% (from 196

to 294 MPa). At 200 ^{o}C, the YS and UTS rose by 45% (160 to 232 MPa) and 48% (from 173 to 256 MPa).

(4) The improved fatigue and mechanical properties in the Zr-modified alloy could closely related to: (1) the refined microstructure, with α-Al grain size decreasing from 335 to 253 μm and the secondary dendrite arm spacing (SDAS) dropping from 39 to 28 μm; (2) the reduced porosity, in particular large sized porosities; (3) the additional Zr-containing precipitates strengthening effect.

Acknowledgement

Financial support from Jaguar Range Rover (JLR) [grant number R33232] is gratefully acknowledged.

References

[1] L. Ceschini, A. Morri, S. Toschi and S. Seifeddine, "Room and high temperature fatigue behaviour of the A354 and C355 (Al–Si–Cu–Mg) alloys: role of microstructure and heat treatment," *Materials Science & Engineering A,* vol. 653, pp. 129-138, 2016.

[2] L. Ceschini, A. Morri, A. T. S. Morri, S. Johansson and S. Seifeddine, "Effect of microstructure and overaging on the tensile behavior at room and elevated temperature of C355-T6 cast aluminum alloy," *Materials & Design,* vol. 83, pp. 626-634, 2015.

[3] C.-Y. Jeong, "High temperature mechanical properties of AlSiMg(Cu) alloys for automotive cylinder heads," *Materials Transactions,* vol. 54, pp. 588-594, 2013.

[4] M. Javidani and D. Larouche, "Application of cast Al–Si alloys in internal combustion engine components," *International Materials Reviews,* vol. 59, pp. 132-158, 2014.

[5] Q. Wang, D. Apelian and D. Lados, "Fatigue behavior of A356-T6 aluminum cast alloys. Part I. Effect of casting defects," *Journal of Light Metals,* vol. 1, pp. 73-84, 2001.

[6] V. Firouzdor, M. Rajabi, E. Nejati and F. Khomamizadeh, "Effect of microstructural constituents on the thermal fatigue life of A319 alluminum alloy," *Materials Science & Engineering A,* Vols. 454-455, pp. 528-535, 2007.

[7] L. Lasa and J. Rodriguez-lbabe, “Toughness and fatigue behaviour of eutectic and hypereutectic Al–Si–Cu–Mg alloys produced through lost foam and squeeze casting,” *Materials Science and Technology,* vol. 20, pp. 1599-1608, 2004.

[8] Y. Gao, J. Yi, P. Lee and T. Lindley, “A micro-cell model of the effect of microstructure and defects on fatigue resistance in cast aluminum alloys,” *Acta Materialia,* vol. 52, pp. 5435-5449, 2004.

[9] H. Elhadari, H. Patel, D. Chen and W. Kasprzak, “Tensile and fatigue properties of a cast aluminum alloy with Ti, Zr and V additions,” *Materials Science and Engineering A,* vol. 528, pp. 8128-8138, 2011.

[10] S. Shaha, F. Czerwinski, W. Kasprzak, J. Friedman and D. Chen, “Improving High-Temperature Tensile and Low-Cycle Fatigue Behavior of Al-Si-Cu-Mg Alloys Through Micro-additions of Ti, V, and Zr,” *Metallurgy and Materials Transactions A,* vol. 46A, pp. 3063-3078, 2015.

[11] S. Shaha, F. Czerwinski, W. F. J. Kasprzak and D. Chen, “Effect of Mn and heat treatment on improvements in static strength and low-cycle fatigue life of an Al–Si–Cu–Mg alloy,” *Materials Science & Engineering A,* vol. 657, pp. 441-452, 2016.

[12] S. Shaha, F. Czerwinski, W. Kasprzak, J. Friedman and D. Chen, “Ageing characteristics and high-temperature tensile properties of Al–Si–Cu–Mg alloys with micro-additions of Mo and Mn,” *Materials Science & Engineering A,* vol. 684, pp. 726-736, 2017.

[13] S. Shaha, F. Czerwinski, W. Kasprzak, J. Frideman and D. Chen, “Monotonic and cyclic deformation behavior of the Al–Si–Cu–Mg cast alloy with micro-additions of Ti, V and Zr,” *International Journal of Fatigue,* vol. 70, pp. 383-394, 2015.

[14] J. Feng, B. Ye, L. Zuo, R. Qi, Q. Wang, H. Jiang and R. Huang, “Effects of Ni content on low cycle fatigue and mechanical properties of Al-12Si-0.9Cu-0.8Mg-xNi at 350 °C,” *Materials Science & Engineering A,* vol. 706, pp. 27-37, 2017.

[15] J. Hernandez-Sandoval, G. Garza-Elizondo, A. Samuel, S. Valtiierra and F. Samuel, “The ambient and high temperature deformation behavior of Al–Si–Cu–Mg alloy with minor Ti, Zr, Ni additions,” *Materials and Design,* vol. 58, pp. 89-101, 2014.

[16] A. Mohamed, F. Samuel and S. Al Kahtani, “Microstructure, tensile properties and fracture behavior of high temperature Al–Si–Mg–Cu cast alloys,” *Materials Science & Engineering A,* vol. 577, pp. 64-72, 2013.

[17] M. Rahimian, S. Amirkhanlou, P. Blake and S. Ji, “Nanoscale Zr-containing precipitates; a solution for significant improvement of high-temperature strength in Al-Si-Cu-Mg alloys,” *Materials Science & Engineering A,* vol. 721, pp. 328-338, 2018.

[18] A. committee, “Standard test methods for tension testing of metallic materials,” 2003.

[19] A. committee, “Standart test methods for tlevated temperature tension tests of metallic materials,” 2003.

[20] A. committee, “Standard practice for conducting force controlled constant amplitude axial fatigue tests of metallic materials,” 2015.

[21] S. Shaha, F. Czerwinski, W. Kasprzak, J. Friedman and D. Chen, “Ageing characteristics and high-temperature tensile properties of Al–Si–Cu–Mg alloys with micro-additions of Cr, Ti, V and Zr,” *Materials Science & Engineering A,* vol. 652, pp. 353-364, 2016.

[22] W. Kasprzak, B. Amirkhiz and M. Niewczas, “Structure and properties of cast Al–Si based alloy with Zr–V–Ti additions and its evaluation of high temperature performance,” *Journal of Alloys and Compounds journal,* vol. 595, pp. 67-79, 2014.

[23] A. Farkoosh and M. Pekguleryuz, “Enhanced mechanical properties of an Al–Si–Cu–Mg alloy at 300 C: Effects of Mg and the Q-precipitate phase,” *Materials Science & Engineering A journal,* vol. 621, pp. 277-286, 2015.

[24] O. Basquin, “The exponential law of endurance tests,” *Proc. Am. Soc. Test. Mater.,* vol. 10, pp. 625-630, 1910.

[25] H. Ammar, A. Samuel and F. Samuel, “Porosity and the fatigue behavior of hypoeutectic and hypereutectic aluminum–silicon casting alloys,” *International Journal of Fatigue,* vol. 30, pp. 1024-1035, 2008.

[26] A. Emami, S. Begum, D. Chen, T. Skszek, X. Niu, Y. Zhang and F. Gabbianelli, “Cyclic deformation behavior of a cast aluminum alloy,” *Materials Science & Engineering A,* vol. 516, pp. 31-41, 2009.

[27] K. Fan, G. He, X. Liu, B. Liu, M. She, Y. Yuan, Y. Yang and Q. Lu, “Tensile and fatigue properties of gravity casting aluminum alloys for engine cylinder heads,” *Materials Science & Engineering A,* vol. 586, pp. 78-85, 2013.

[28] J. Zhou, S. Huang, J. Sheng, J. Lu, C. Wang, K. Chen, H. Ruan and H. Chen, “Effect of repeated impacts on mechanical properties and fatigue fracture morphologies of 6061-T6

aluminum subject to laser peening," *Materials Science & Engineering A,* vol. 539, pp. 360-368, 2012.

[29] M. Easton and D. StJohn, "An Analysis of the relationship between grain size, solute content, and the potency and number density of nucleant Particles," *Metallurgical and Materials Transactions A,* vol. 36, pp. 1911-1920, 2005.

[30] D. StJohn, M. Qian, M. Easton and P. Cao, "The Interdependence Theory: The relationship between grain formation and nucleant selection," *Acta Materialia,* vol. 59, pp. 4907-4921, 2011.

[31] M. Easton and D. StJohn, "Grain refinement of aluminum alloys: Part II. Confirmation of, and a mechanism for, the solute paradigm," *Metallurgical and Materials Transactions A,* vol. 30, pp. 1625-1633, 1999.

[32] M. S. D. Easton, "Improved prediction of the grain size of aluminum alloys that includes the effect of cooling rate," *Materials Science & Engineering: A,* vol. 486, pp. 8-13, 2008.

[33] F. Wang, Z. Liu, D. Qiu, J. Taylor, M. Easton and M. Zhang, "Revisiting the role of peritectics in grain refinement of Al alloys," *Acta Materialia,* vol. 61, pp. 360-370, 2013.

[34] T. Quested, A. Dinsdale and A. Greer, "Thermodynamic modelling of growth-restriction effects in aluminium alloys," *Acta Materialia,* vol. 53, pp. 1323-1334, 2005.

[35] W. F., Z. Liu, D. Qiu, J. Taylor, M. Easton and M. Zhang, "Revisiting the role of peritectics in grain refinement of Al alloys," *Acta Materialia,* vol. 61, pp. 360-370, 2013.

[36] F. Wang, D. Qiu, Z. Liu, J. Taylor, M. Easton and M. Zhang, "The grain refinement mechanism of cast aluminium by zirconium," *Acta Materialia,* vol. 61, pp. 5636-5645, 2013.

[37] M. Colombo, E. Gariboldi and A. Morri, "Influences of different Zr additions on the microstructure, room and high temperature mechanical properties of an Al-7Si-0.4Mg alloy modified with 0.25%Er," *Materials Science & Engineering A,* vol. 713, pp. 151-160, 2018.

[38] H. Ye, "An overview of the development of Al-Si-Alloy based material for engine applications," *Journal of Materials Engineering and Performance,* vol. 12, pp. 288-297, 2003.

[39] E. Hall, "The deformation and ageing of mild steel: III discussion of results," *Proceedings of the Physical Society,* vol. 64, pp. 747-752, 1951.

[40] N. Petch, “The cleavage strength of polycrystals,” *Journal of the Iron and Steel Institute,* Vols. 25-28, p. 174, 1953.

[41] X. Dong, Y. Zhang, S. Amirkhanlou and S. Ji, “High performance gravity cast Al9Si0.45Mg0.4Cu alloy inoculated with AlB2 and TiB2,” *Journal of Materials Processing and Technology,* vol. 252, pp. 604-611, 2018.

[42] K. Kending and D. Miracle, “Strengthening mechanisms of an Al-Mg-Sc-Zr alloy,” *Acta Materialia,* vol. 50, pp. 4165-4175, 2002.

[43] Y. Zheng, W. Xiao, S. Ge, W. Zhao, S. Hanada and C. Ma, “Effects of Cu content and Cu/Mg ratio on the microstructure and mechanical properties of Al-Si-Cu-Mg alloys,” *Journal of Alloys and Compounds,* vol. 649, pp. 291-296, 2015.

[44] P. Hunter, P. Renhart, S. Oberfrank, M. Schwab, F. Grun and B. Stauder, “High- and low-cycle fatigue influence of silicon, copper, strontium and iron on hypo-eutectic Al–Si–Cu and Al–Si–Mg cast alloys used in cylinder heads,” *International Journal of Fatigue,* vol. 82, pp. 588-601, 2016.

[45] B. Zhang, D. Poirier and W. Chen, “Microstructural effects on high-cycle fatigue-crack initiation in A356.2 casting alloy,” *Metallurgical and Materials Transactions A,* vol. 30, pp. 2659-2665, 1999.

[46] S. Jana, R. Mishra, J. Baumann and G. Grant, “Effect of friction stir processing on fatigue behavior of an investment cast Al–7Si–0.6 Mg alloy,” *Acta Materialia,* vol. 58, pp. 989-1003, 2010.

[47] S. Dezecot, V. Maurel, J. Buffiere, F. Szmytca and A. Koster, “3D characterization and modeling of low cycle fatigue damage mechanisms at high temperature in a cast aluminum alloy,” *Acta Materialia,* vol. 123, pp. 24-34, 2017.

[48] D. Lados and D. Apelian, “Fatigue crack growth characteristics in cast Al–Si–Mg alloys Part I. Effect of processing conditions and microstructure,” *Materials Science & Engineering A,* vol. 385, pp. 200-211, 2004.

[49] F. Lee, J. Major and F. Samuel, “Effect of silicon particles on the fatigue crack growth characteristics of Al-12 Wt Pct Si-0.35 Wt Pct Mg-(0 to 0.02) Wt Pct Sr casting alloys,” *Metallurgical and Materials Transactions A,* vol. 26, pp. 1553-1570, 1995.

Table 1 Chemical composition of the experimental Al-Si-Cu-Mg alloys measured by inductively coupled plasma atomic emission spectroscopy (ICP-AES), wt.%.

Alloys	Al	Si	Cu	Mg	Ti	Zr	Mn	Cr	Fe	Ni	V	Zn	Sr
Baseline	Rem	6.79	0.51	0.35	0.11	0.002	0.008	0.001	0.09	0.004	0.017	0.008	0.015
Zr-modified	Rem	8.59	0.79	0.37	0.12	0.14	0.008	0.001	0.10	0.004	0.010	0.010	0.017

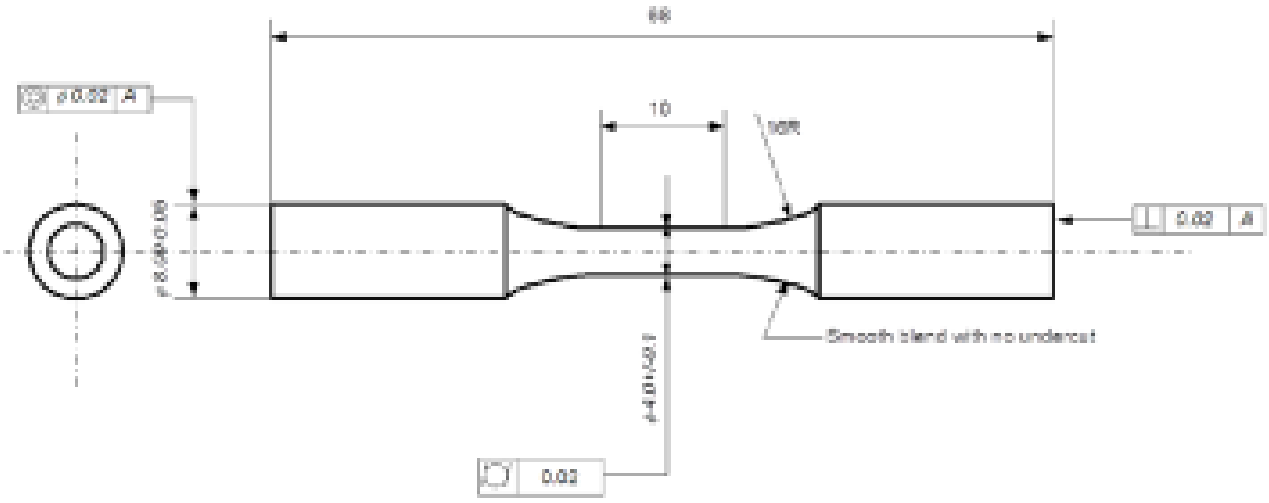

Figure 1 The geometry and dimension of the specimen subjected to the high cycle fatigue test.

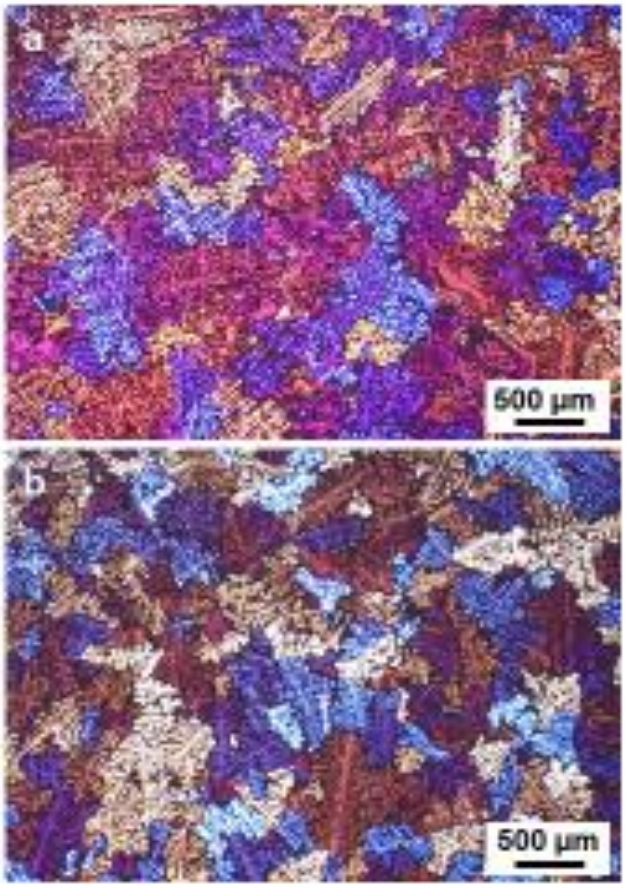

Figure 2 Optical micrographs showing the grain size of (a) baseline, and (b) Zr-modified Al-Si-Cu-Mg alloys after T6 heat treatment.

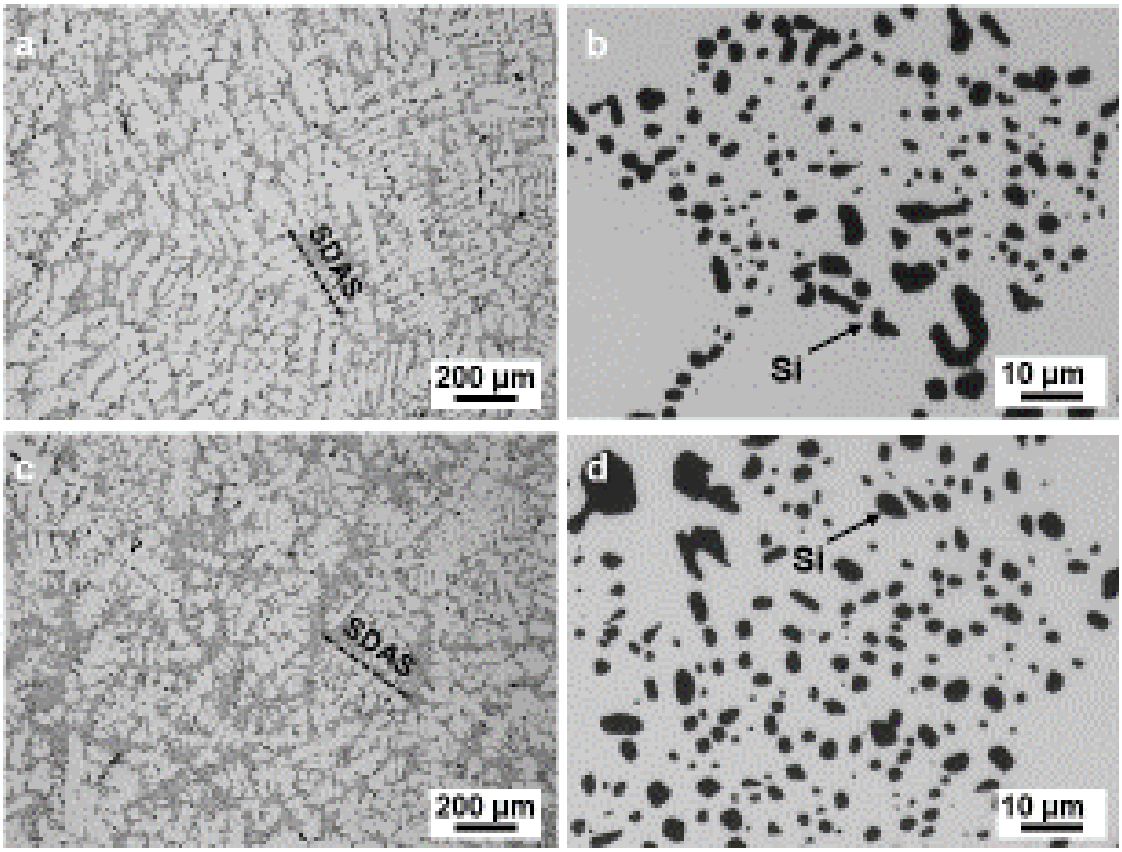

Figure 3 Optical micrographs showing the primary α-Al and eutectic Si phases of (a, b) baseline, and (c, d) Zr-modified Al-Si-Cu-Mg alloys after T6 heat treatment.

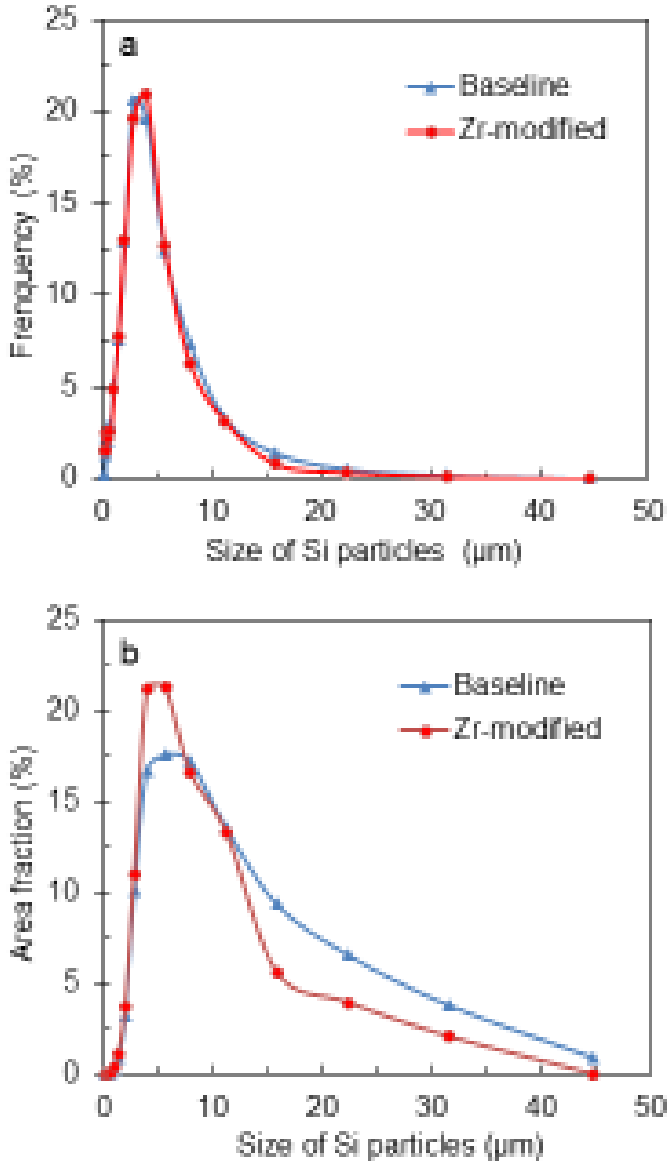

Figure 4 The size distribution of the Si particles of the baseline and Zr-modified Al-Si-Cu-Mg alloys after T6 heat treatment. (a) number fraction, and (b) area fraction. More than 10000 individual Si particles were statistically measured.

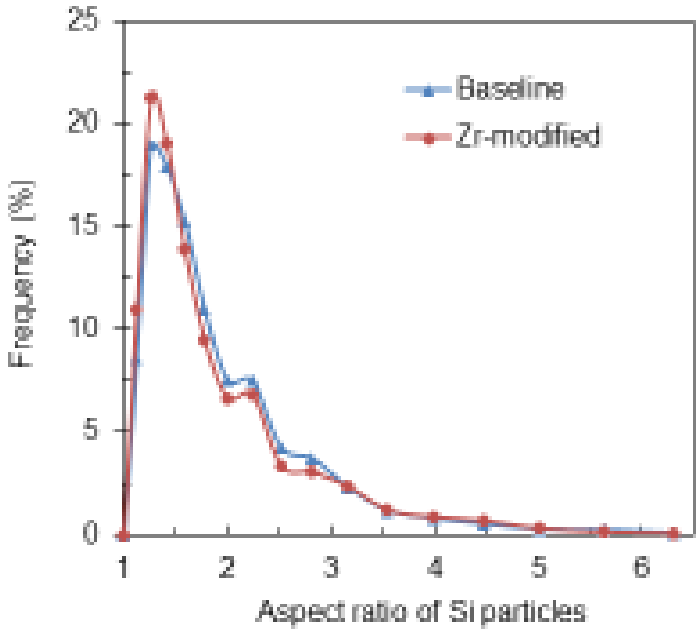

Figure 5 The aspect ratio distribution of the Si particles of the baseline and Zr-modified Al-Si-Cu-Mg alloys after T6 heat treatment. More than 10000 individual Si particles were statistically measured.

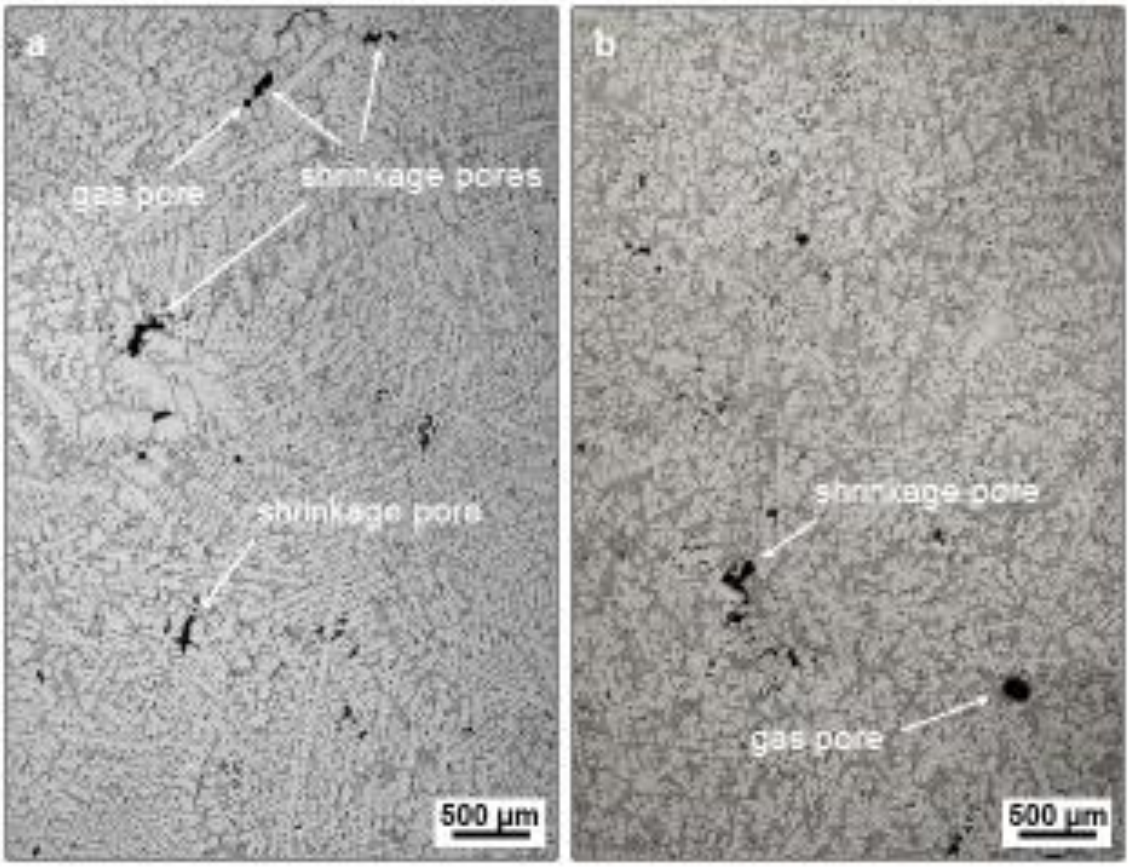

Figure 6 Optical micrographs showing the gas and shrinkage pores of (a) the baseline and (b) Zr-modified Al-Si-Cu-Mg alloys after T6 heat treatment.

Table 2 Comparison of the quantitative metallographic characteristics of α-Al, eutectics, Si particles, and porosities of the experimental Al-Si-Cu-Mg alloys. GS: Grain size, SDAS: Secondary dendrite arm spacing.

Alloys	α-Al		Eutectics	Si particles		Porosities		
	GS (μm)	SDAS (μm)	Area fraction (%)	Mean Ferret diameter (μm)	Mean aspect ratio	Area fraction (%)	Mean aspect ratio	Mean Ferret diameter (μm)
Baseline	335±18	30±2	27.8±1.2	3.3±1.9	1.65±0.44	0.33±0.02	2.4±0.1	110.2±11.2
Zr-modified	253±41	26±3	33.1±0.9	3.1±1.7	1.61±0.44	0.31±0.03	2.0±0.2	106.1±9.6

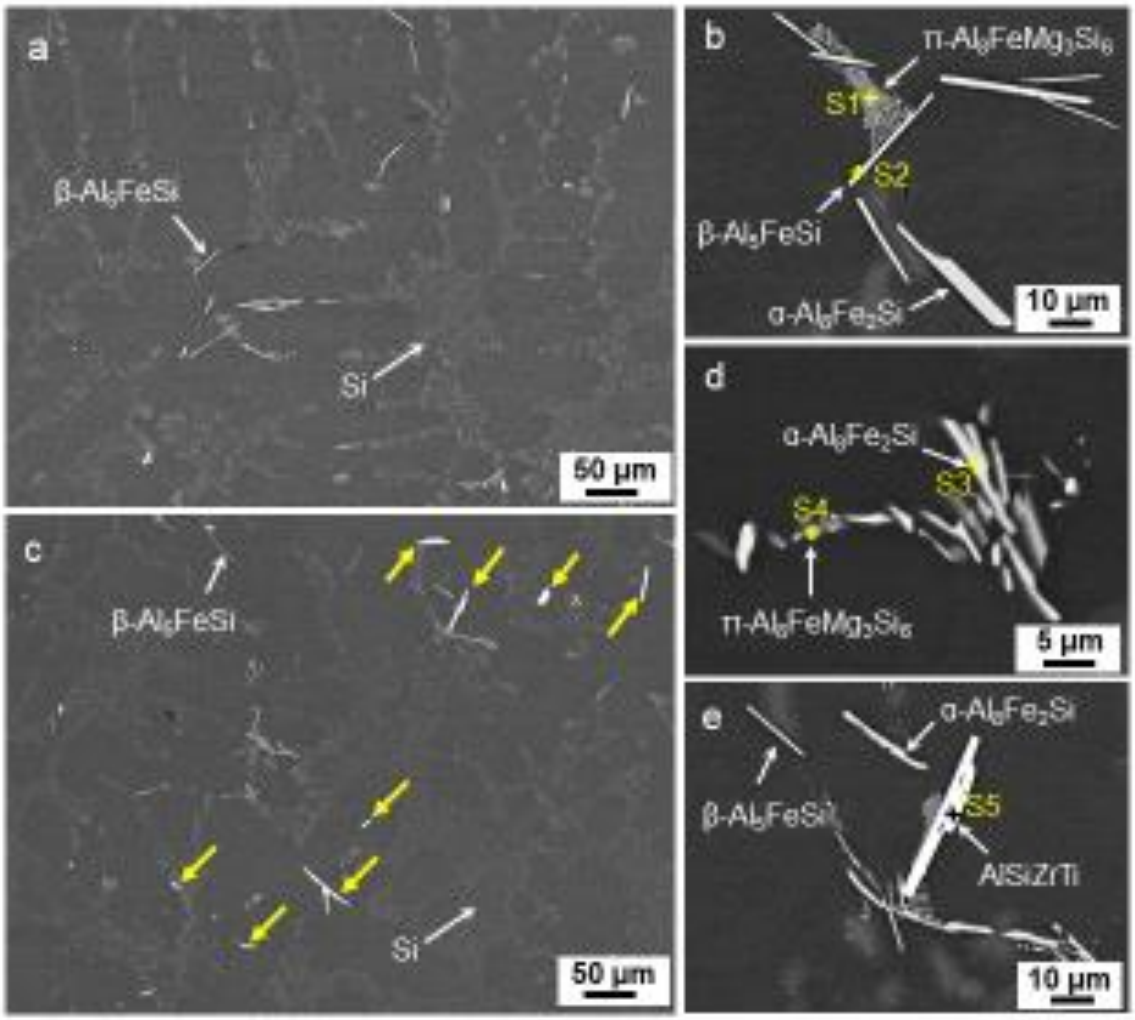

Figure 7 BSE-SEM micrographs showing the Fe-rich and Zr-containing intermetallic phases in the Al-Si-Cu-Mg alloys after T6 heat treatment: (a, b) baseline, and (c, d, e) Zr-modified.

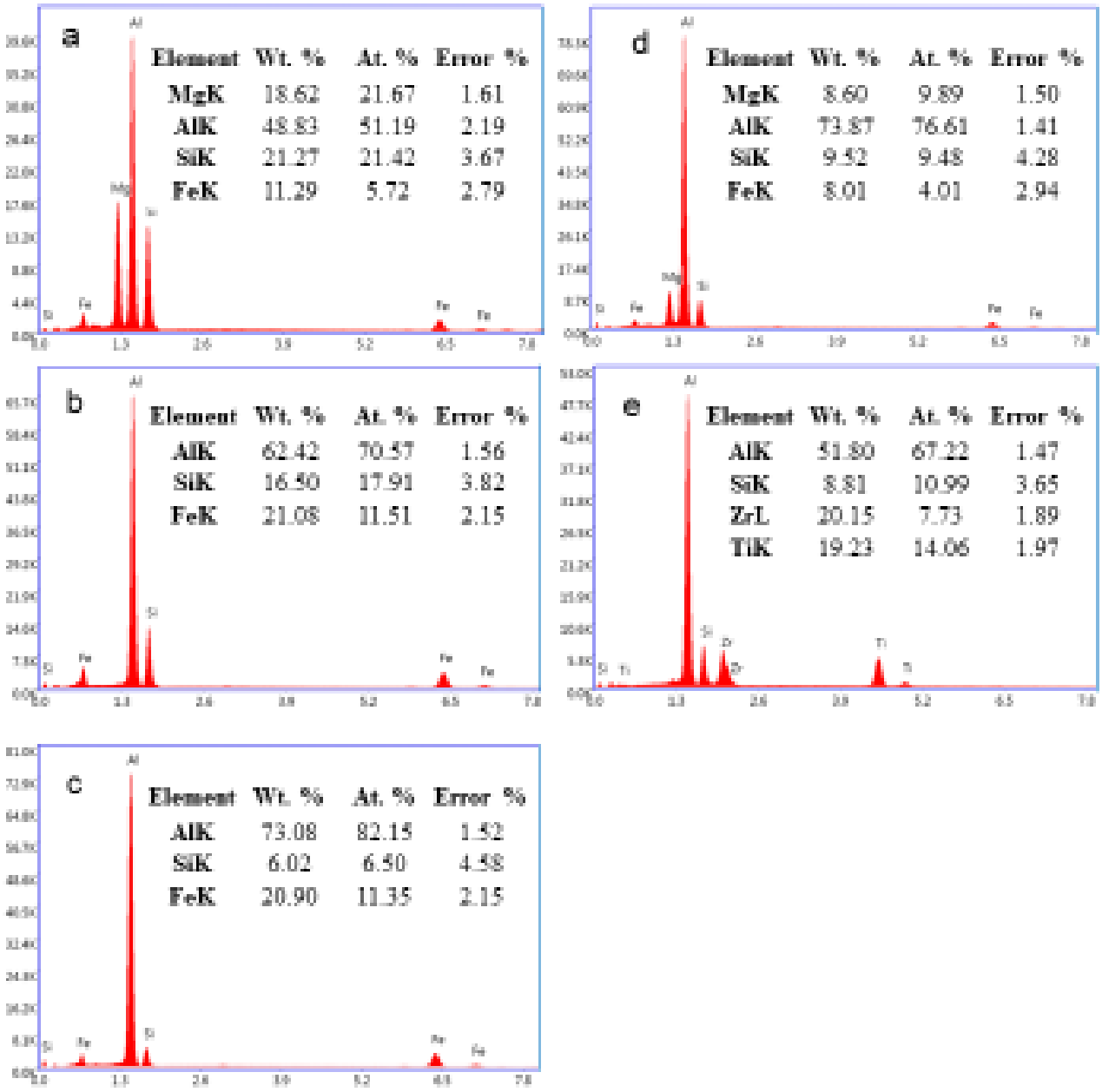

Figure 8 EDS analysis of the Fe-rich and Zr-containing intermetallic phases corresponding to the spectrums in Figure 7: (a) S1, (b)S2, (c) S3, (d) S4, and (e) S5.

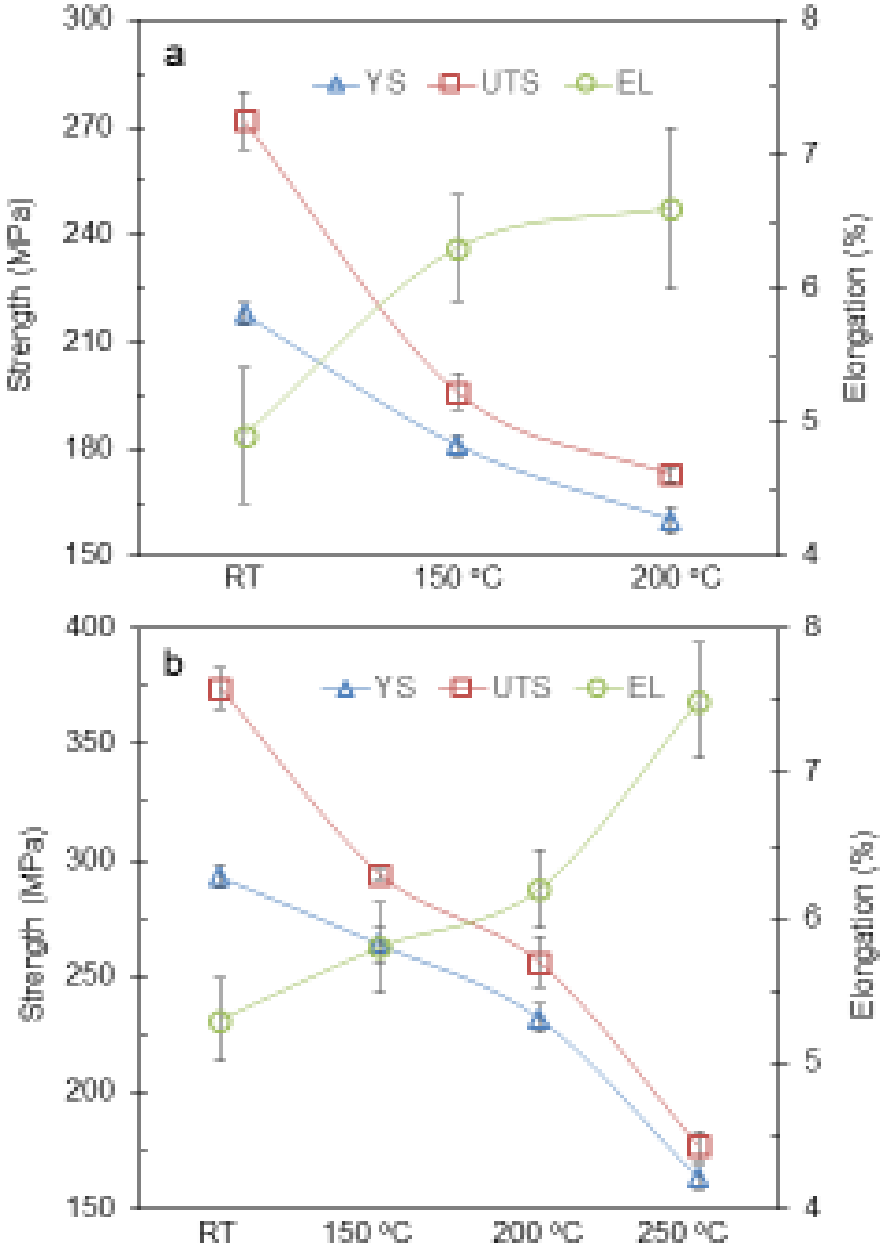

Figure 9 Tensile properties of (a) the baseline and (b) Zr-modified Al-Si-Mg-Cu alloys at different temperatures, RT: room temperature.

Table 3 The tensile properties of the baseline and Zr-modified Al-Si-Cu-Mg alloys tested at room and elevated temperatures.

Alloys	Test conditions	YS (MPa)	UTS (MPa)	EL (%)
Baseline	RT	218	272	4.9
	150 °C	181	196	6.3
	200 °C	160	173	6.6
Zr-modified	RT	293	374	5.3
	150 °C	264	294	5.8
	200 °C	232	256	6.2
	250 °C	163	177	7.5

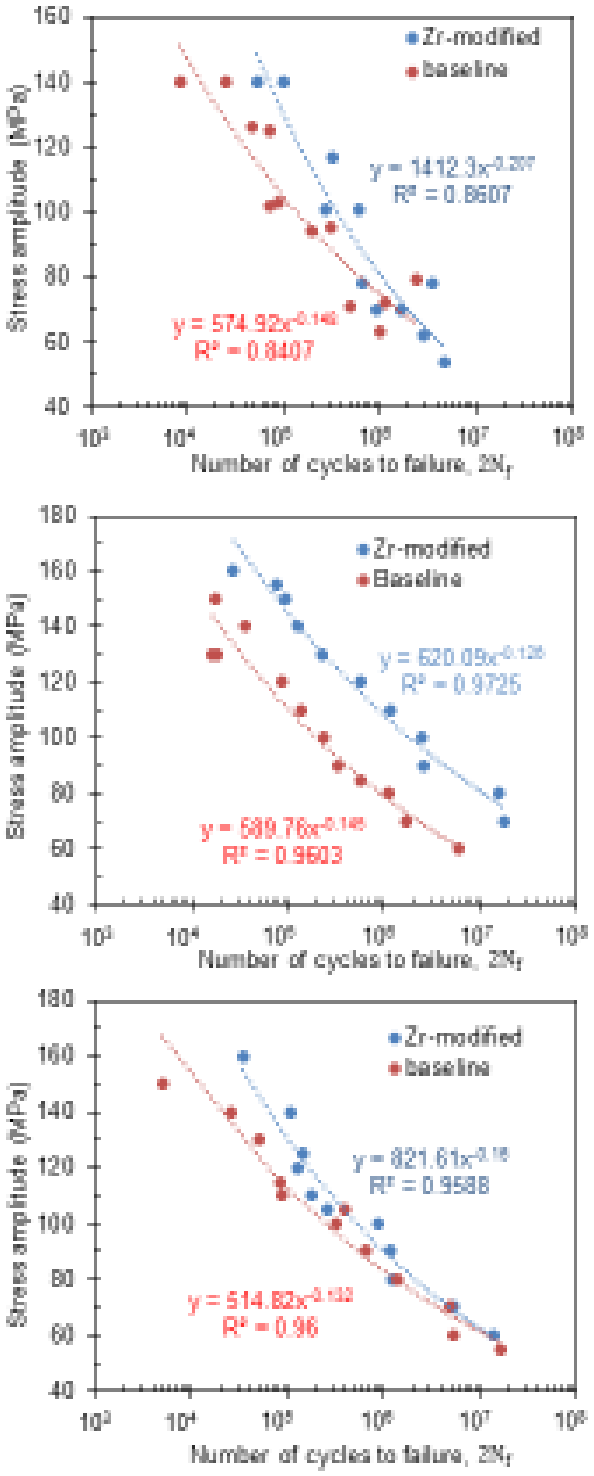

Figure 10 S-N curves of the baseline and Zr-modified Al-Si-Mg-Cu alloys tested at (a)150 °C, (b) 200 °C, and (c) 250 °C.

Table 4 The fatigue strength coefficient (σ_f') and fatigue strength exponent (b) of the baseline and Zr-modified Al-Si-Cu-Mg alloys tested at 150, 200, and 250 °C, $\sigma_a = \sigma_f' (2N_f)^b$.

Materials	150 °C			200 °C			250°C		
	σ_f' (MPa)	b	R^2	σ_f' (MPa)	b	R^2	σ_f' (MPa)	b	R^2
Baseline	574.9	-0.148	0.841	589.8	-0.145	0.960	514.8	-0.132	0.960
Zr-modified	1412.3	-0.207	0.861	620.1	-0.126	0.973	821.6	-0.160	0.959

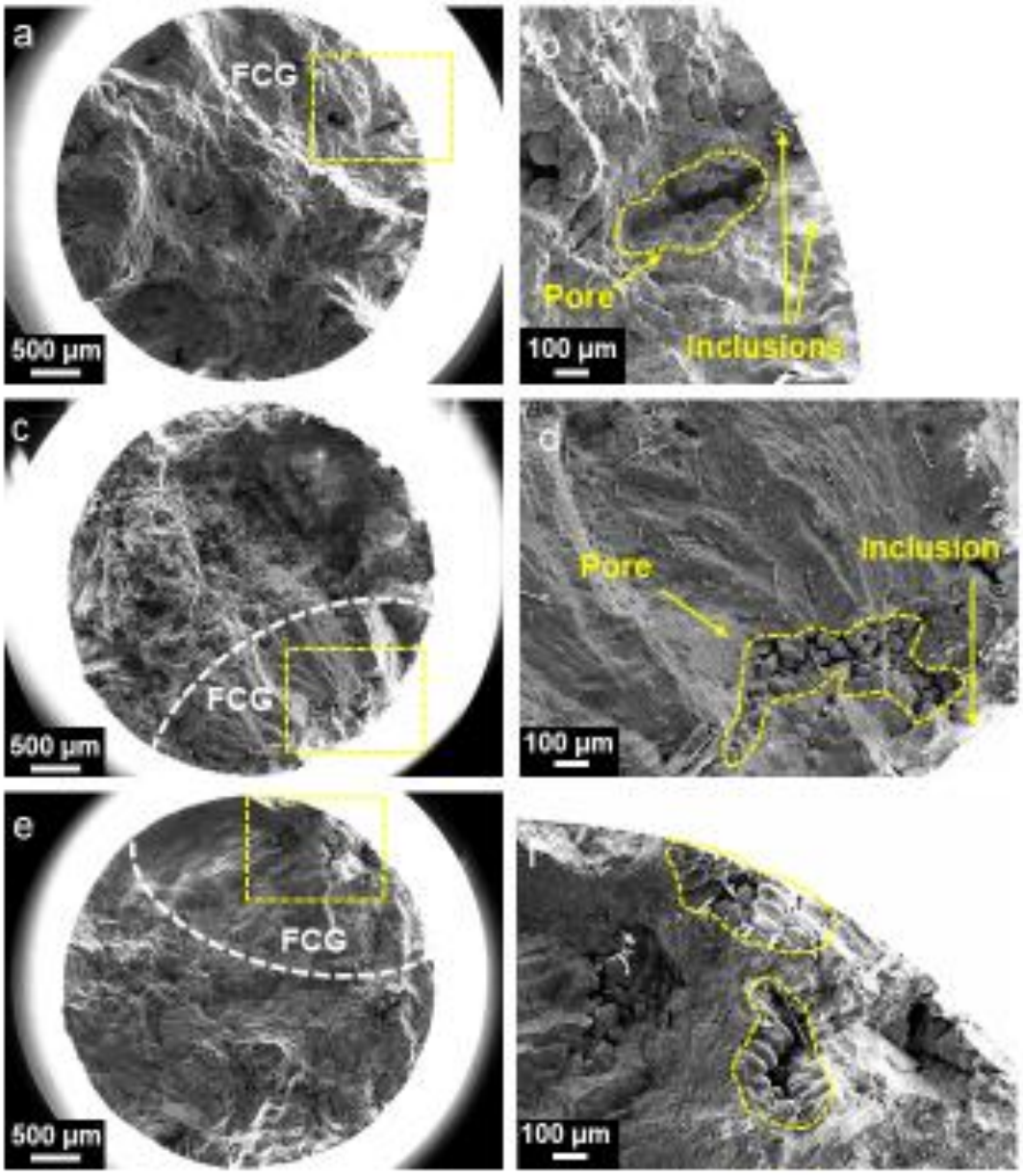

Figure 11 SEM micrographs showing the fatigue fracture surface of the baseline Al-Si-Cu-Mg alloys tested at 200 °C under different stress amplitudes of (a, b) 150 MPa, (c, d) 100 MPa, and (e, f) 70 MPa. FCG: Fatigue crack growth, FCI: Fatigue crack initiation.

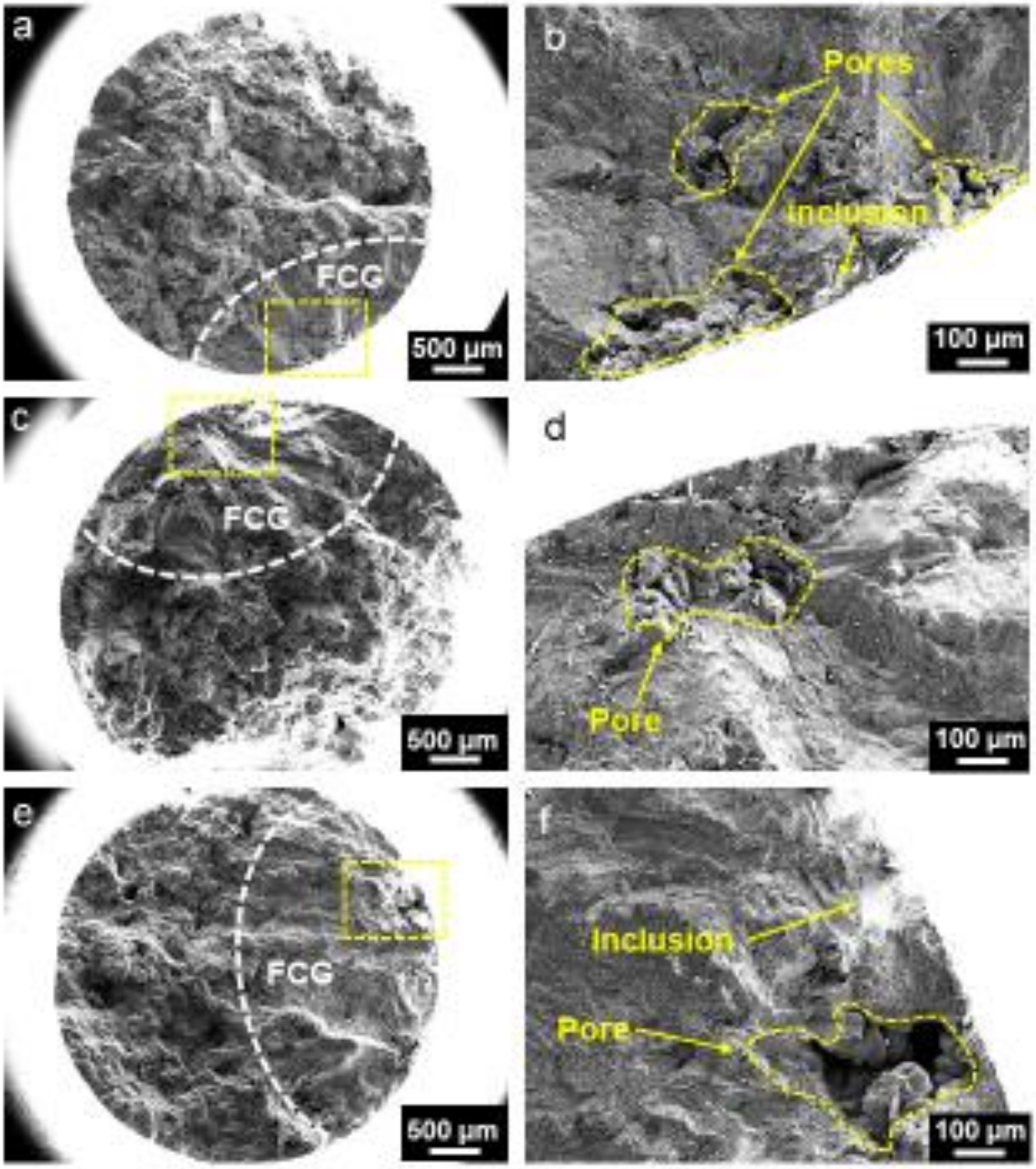

Figure 12 SEM micrographs showing the fatigue fracture surface of the Zr-modified Al-Si-Cu-Mg alloys tested at 200 °C under different stress amplitudes of (a, b) 150 MPa, (c, d) 100 MPa, and (e, f) 70 MPa. FCG: Fatigue crack growth, FCI: Fatigue crack initiation.

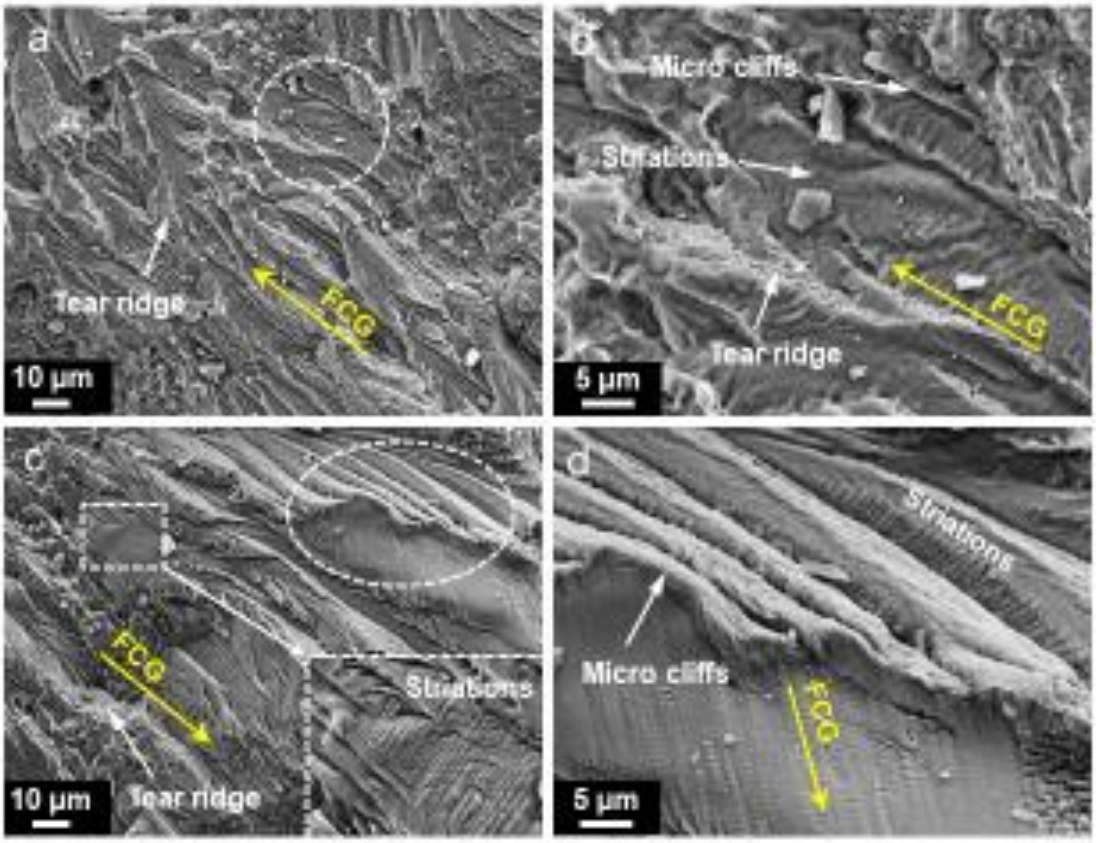

Figure 13 SEM micrographs of fatigue fracture surface, showing the fatigue crack growth of (a, b) the baseline and (c, d) Zr-modified Al-Si-Cu-Mg alloys tested at 200 °C under fatigue stress amplitudes of 100 MPa. FCG: Fatigue crack growth.

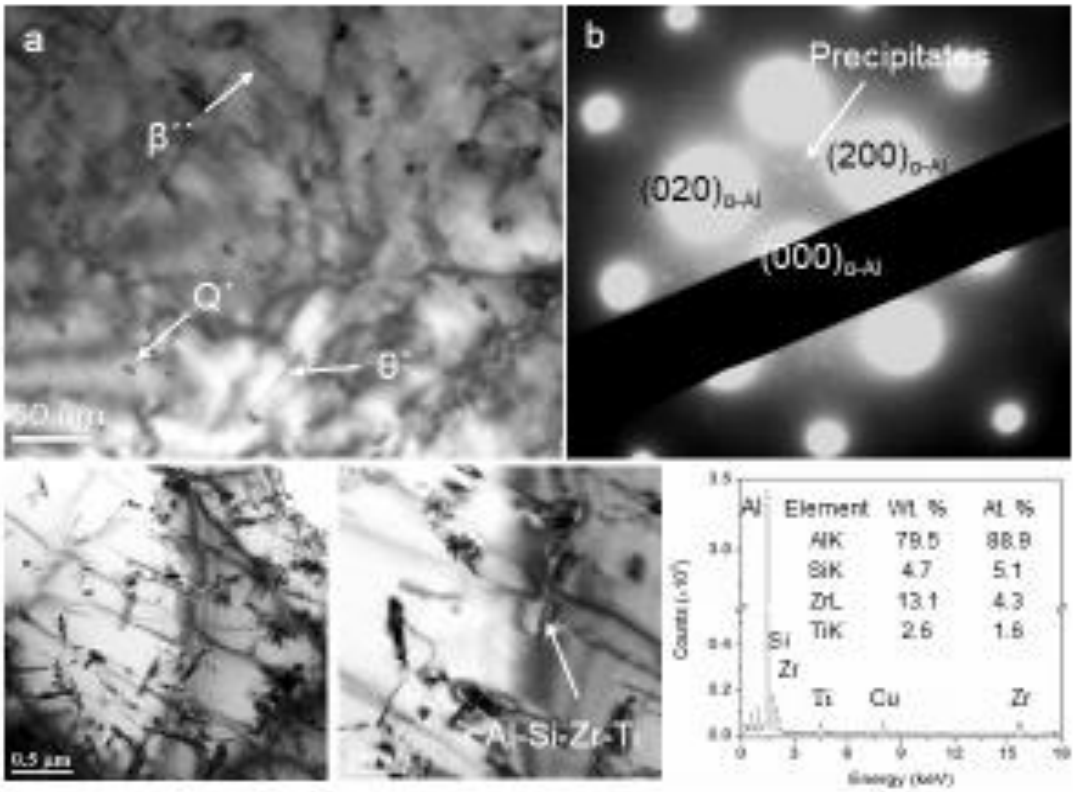

Figure 14 Bright-field TEM micrographs and EDS results, showing (a) the β'', θ', and Q' precipitate phases and (b) corresponding SADP in the baseline Al-Si-Cu-Mg alloy; (c, d) the Al-Si-Zr-Ti precipitates in the Zr-modified Al-Si-Cu-Mg alloy, (e) the EDS results corresponding to the spectrum marked in (d).